Chapter 5

Hydroxyapatite based Functionally Graded Materials

As the polarization in bone plays a very important role in controlling / regulating the various metabolic activities, this chapter aims to increase the polarizability of hydroxyapatite while keeping its surface chemistry intact. Such increase in polarizability without compromising the surface chemistry has been achieved by means of development of functionally graded materials (FGM). The FGMs has been developed by inserting barium titanate (BT) and calcium titanate (CT) layers between the hydroxyapatite layers by means of buffer interlayers. The consolidation of the developed FGM is carried out via spark plasma sintering route. Further, the microstructural analyses were carried out for the developed FGMs to observe their structural integrity. Thereafter, dielectric and electrical characterizations such as dielectric constant, loss and ac conductivity analyses were carried out over wide temperature (35°C - 500°C) and frequency (1 kHz - 1 MHz) range. In addition, detailed impedance spectroscopic analyses were also carried out over a similar range of temperatures and frequencies. Overall, the developed FGMs can be suggested as potential materials for polarized bone applications.

5.1. Functionally graded materials for orthopaedic applications

Due to the structural and compositional resemblance with the mineral component of natural bone, hydroxyapatite (HA) is considered to be the promising replacement material as compared to other orthopaedic implant material.[1,2] In addition, polarization of HA via external electrical stimulation can significantly improve/accelerate the normal bone functionality as well as osseointegration *in-vitro* and *in-vivo*.[3,4,5] It is mentioned that human bone is a piezoelectric material and this property further affects the biochemical processes which results in reconstruction / remodelling and growth of bone tissue.[6,7,8] The pervoskite, $BaTiO_3$ (BT) is one of the piezoelectric ceramics which has been revealed to be a likely

prospective orthopaedic implant in the number of *in-vitro* and *in-vivo* studies.[9,10,11,12] Also, addition of $BaTiO_3$ in hydroxyapatite (HA) as a reinforcement phase has been reported to enhance the electrical properties such as dielectric constant, piezoelectric and pyroelectric coefficients [13,14] with appreciable improvement in the mechanical properties such as fracture toughness[15], compressive strength and modulus of the composite system. A composite of $BaTiO_3$ with poly (vinylidene-trifluoroethylene) has been suggested to significantly improve the response of human osteoblast cells in terms of cell proliferation and viability as compared to mere polymer matrix.[16] Also, the application of electrical stimulation as well as polarization treatment of HA-$BaTiO_3$ composites has been demonstrated to significantly improve the growth and proliferation of mouse fibroblast (L929) and osteogenic cells.[17] Another pervoskite, $CaTiO_3$ (CT) has also been observed to be a potential biocompatible material.[18] It provides enhanced osteoblast cell adhesion and increased osteointegration.[19] Composites of HA-$CaTiO_3$ (HA-80 wt %) has been reported to demonstrate superior biocompatibility as compared to monotlithic HA, after implantation in the femoral bone defects in the rabbit animal model.[20] It has also been shown that the composites of HA-$CaTiO_3$ prepared via spark plasma sintering route exhibits, higher conductivity [$\sim 10^{-5}$ (ohm cm)$^{-1}$] as compared to conventional sintering route [$\sim 10^{-8}$ (ohm cm)$^{-1}$], which can mimic the electroactive properties of the bone.[21]

As far as development of HA-based composites are concerned, the excellent biocompatibility of HA i.e., its surface chemistry is sacrificed. In view of above, the development of FGMs has been carried out comprising of HA using $BaTiO_3$ and $CaTiO_3$ as intermediary layers (Fig. 5.1). The intention to develop such a graded structure is to increase the polarizability of HA without any effect on its surface chemistry i.e., on excellent biocompatibility. In order to reduce the thermal stress at the interface between HA and $BaTiO_3$ layers as well as HA and $CaTiO_3$ layers, an optimized composition of buffer layers have been introduced between these

layers. The buffer layer compensates the thermal mismatch between HA, $BaTiO_3$ as well as HA, $CaTiO_3$ layers. In order to effectively integrate these layers, spark plasma sintering route have been adapted to process these samples.

5.2. Experimental details

5.2.1. Synthesis

Hydroxyapatite [$Ca_{10}(PO_4)_6(OH)_2$, HA] powder was synthesized via wet precipitation route using stoichiometric amounts of aqueous solutions of calcium oxide (CaO) and ortho-phosphoric acid (H_3PO_4) as precursors. The aqueous solution of H_3PO_4 (9.5 vol. %) was added drop wise into the aqueous solution of CaO (10 mol.) at fixed temperature (80˚C). The molar ratio of calcium to phosphorus in the pure hydroxyapatite powder was 1.67, which was maintained during the synthesis. The preparation of HA follows the simple reaction,[22]

$$10Ca(OH)_2 + 6H_3PO_4 \rightarrow Ca_{10}(PO_4)_6(OH)_2\downarrow + 18H_2O \quad (5.1)$$

The reaction between the precursors takes place in the basic medium (pH~ 8-10). After overnight cooling, precipitate was then filtered out, dried and calcined at 800˚C for 2 h. $BaTiO_3$ and $CaTiO_3$ were prepared using solid state ceramic route. For preparation of $BaTiO_3$, stoichiometric amounts of $BaCO_3$ and TiO_2 were mixed and ball milled for 24h in polyethylene jar using zirconia balls (5 mm dia) and acetone as milling medium. For synthesis of $CaTiO_3$, $CaCO_3$ and TiO_2 were used as precursors. The weight ratio of balls to powder mixture was taken as 4:1 in each case. After milling, the filtered samples were dried, crushed and calcined. $BaTiO_3$ and $CaTiO_3$ powders were calcined at 1000˚C (6 h) and 1150˚C (8 h), respectively. As the coefficients of thermal expansion for HA, $BaTiO_3$ and $CaTiO_3$ are different, a buffer layer between HA/$BaTiO_3$ and HA/$CaTiO_3$ layers has been introduced to avoid the thermal mismatch during sintering. The optimized buffer layer composition was observed to contain the equal amounts of HA and $BaTiO_3$ or HA and $CaTiO_3$ components.

The preparation of HA and FGM samples was carried out using spark plasma sintering (SPS) route. Two different FGMs, with the layer arrangements as HA-buffer-$BaTiO_3$-buffer-HA [Fig. 5.1(a)] as well as HA-buffer-$CaTiO_3$-buffer-HA [Fig. 5.1(b)] have been developed. The stacked layers were pressed at 50 MPa in the graphite die and sintered at 1100˚C for 10 min using SPS with heating rate of 50˚C min^{-1}. The diameter and thickness of spark plasma sintered samples were 15 mm and 2 mm, respectively.

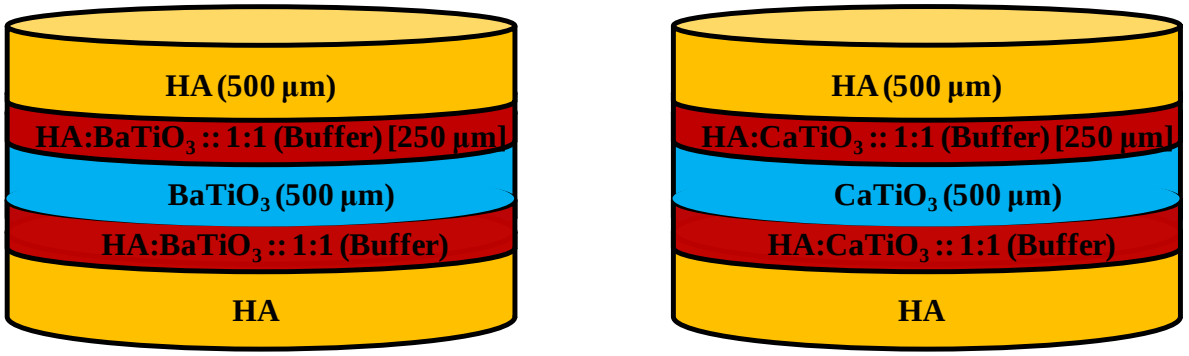

(a) **(b)**

Fig. 5.1: Spatial distribution of different layers in developed FGM, (a) HA:BT:HA and (b) HA:CT:HA

5.2.2. Phase evaluation and microstructural characterization

Phase analyses of all the sintered samples were carried out using X-ray diffraction patterns (Rigaku Miniflex II Desktop X-ray Diffractometer), recorded with the angle of diffraction ranging from 20˚ to 80˚ using Cu-Kα radiation. The diffraction peaks were indexed using the JCPDS data. The morphological analyses of different layers of developed FGMs and their interfaces were carried out using scanning electron microscopy (SEM) and energy dispersive X-ray spectroscopy (EDAX) for fractured surfaces.

5.2.3. Dielectric and electrical characterization

Dielectric and electrical characterization of HA and FGM samples were carried out using Alpha high performance frequency analyser. For this purpose, samples were mirror polished, electroded with Ag paste and cured at 600˚C for 5 min. Electroded samples were then heated at 5 ˚C min^{-1} from room temperature to 500˚C and data was recorded for the dielectric constant ($\varepsilon_r = \frac{Cd}{\varepsilon_o A}$, where C is capacitance of the sample, *d* and *A* are the thickness and area of the samples, respectively, and ε_o is the permittivity of free space) and ac conductivity ($\sigma_{ac} = \frac{Gd}{A}$, *G* is the conductance; $G = \omega CD, \omega = 2\pi f$ is the angular frequency and *D* is the dielectric loss) over the frequency range of 1 Hz to 1 MHz. Further, the detailed impedance analyses were performed.

5.3. Results and discussion

5.3.1. Phase evolution and microstructural analyses

Fig. 5.2(a) represents the XRD patterns of HA, $BaTiO_3$ and buffer composite, containing equal amounts of HA and $BaTiO_3$. The XRD pattern for HA suggests the formation of single hexagonal phase. The tetragonal phase of perovskite $BaTiO_3$ is obtained with complete dissociation of precursors at calcination temperature of 1000˚C, as depicted in Fig 5.2(a). The XRD pattern of buffer signifies the presence of both the constituent phases only. Fig. 5.2(b) represents the XRD patterns of HA, $CaTiO_3$ and buffer composite (HA and $CaTiO_3$). The similar pattern for $CaTiO_3$ has been observed to be orthorhombic perovskite phase and that of buffer signifies the presence of both constituent phases only.

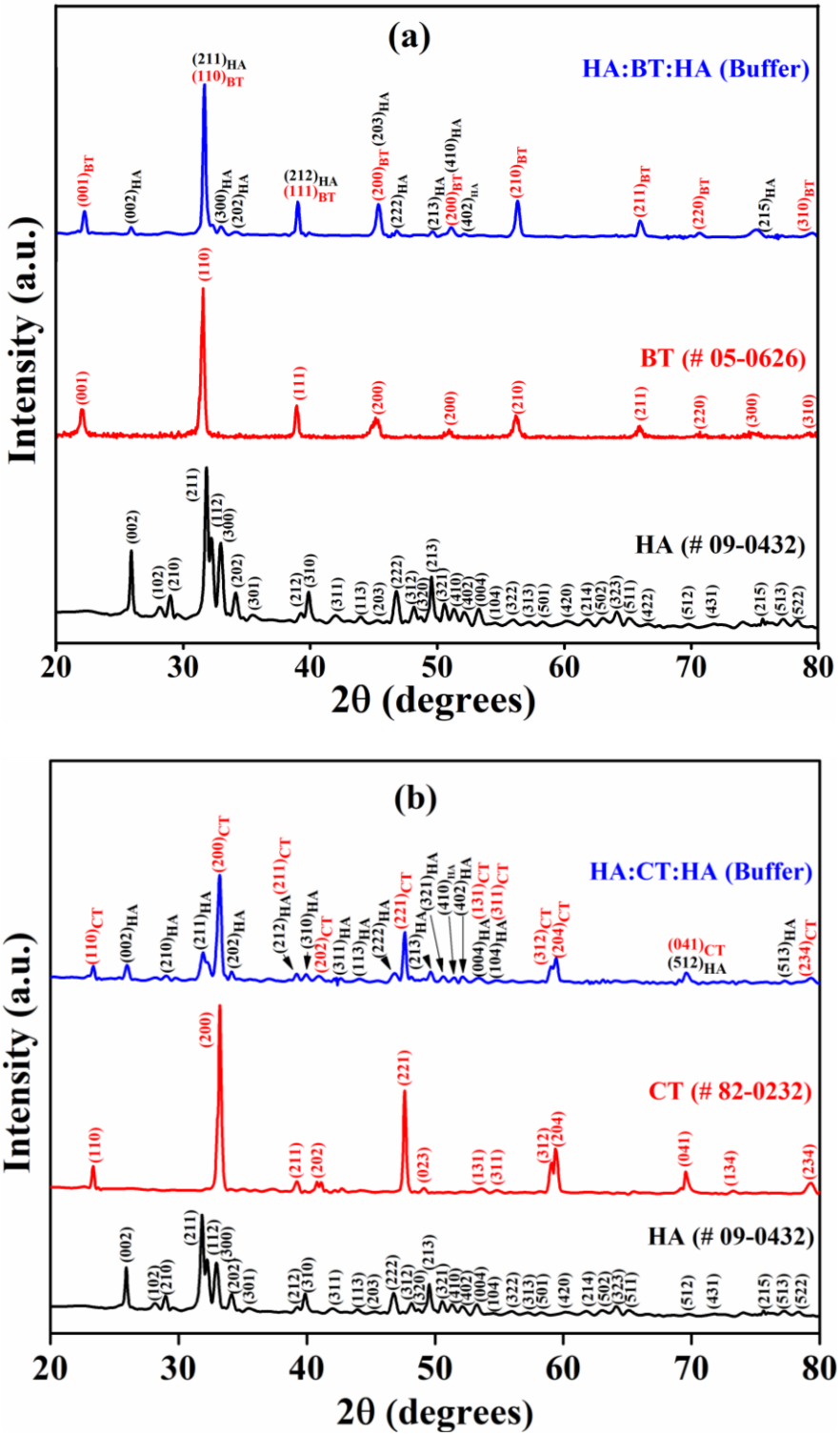

Fig. 5.2: X-Ray diffraction spectra for (a) HA, BT and FGM HA-BT-HA as well as (b) HA, CT and FGM HA-CT-HA samples.

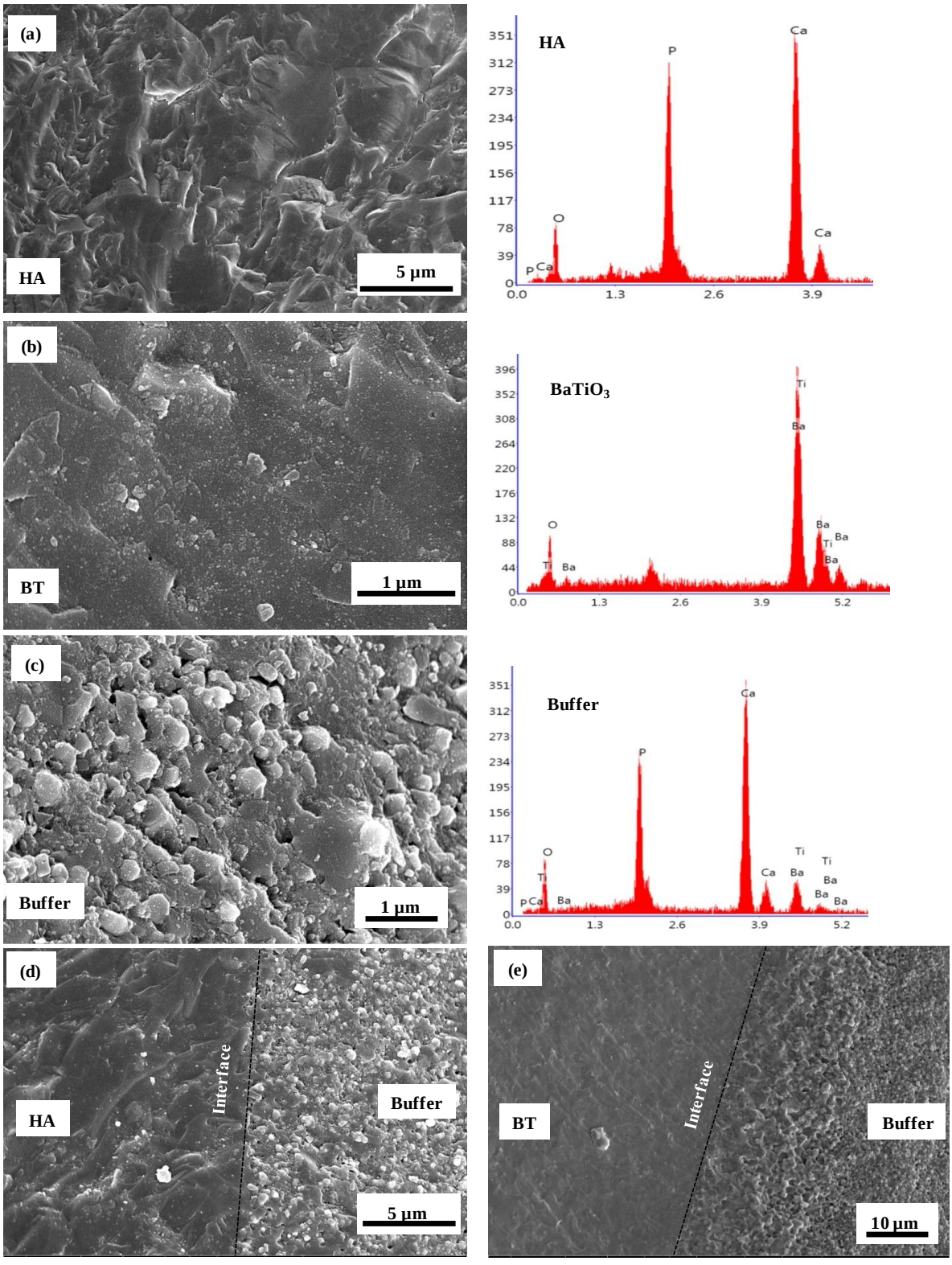
(a)
HA
5 µm
HA
(b)
BT
1 µm
BaTiO3
(c)
Buffer
1 µm
Buffer
(d)
HA
Interface
Buffer
5 µm
(e)
BT
Interface
Buffer
10 µm

HA

Element	Wt %	Atomic %	Error %
O K	37.68	58.06	14.55
P K	19.95	15.88	4.93
CaK	42.37	26.06	3.76

BT

Element	Wt %	Atomic %	Error %
O K	15.91	51.21	13.87
BaL	59.43	22.29	7.55
TiK	24.66	26.51	5.52

Buffer

Element	Wt %	Atomic %	Error %
O K	33.15	55.70	14.89
P K	16.48	14.31	5.83
CaK	38.08	25.54	4.00
BaL	6.68	1.31	37.42
TiK	5.61	3.15	15.86

Fig. 5.3: SEM micrographs illustrating the morphological behaviour of fractured surfaces of (a) HA, (b) BT and (c) buffer, interfacial regions between (d) HA and buffer as well as (e) BT and buffer.

Figs. 5.3 and 5.4 demonstrate the SEM images of fractured surfaces of HA, buffer (HA-$BaTiO_3$ and HA-$CaTiO_3$), $BaTiO_3$ and $CaTiO_3$. The interfacial regions between HA-buffer, $BaTiO_3$-buffer and $CaTiO_3$-buffer are also captured using SEM. The intergranular as well as transgranular modes of fracture are obtained to occur in HA [Fig. 5.3(a)]. The SEM images of HA-$BaTiO_3$-HA FGM [Figs. 5.3 (d) and (e)] and HA-$CaTiO_3$-HA FGM [Figs. 5.4 (d) and (e)] reveal no crack at the interfaces of the HA-buffer, $BaTiO_3$-buffer (for HA-$BaTiO_3$-HA) and HA-buffer as well as $CaTiO_3$-buffer (for HA-$CaTiO_3$-HA). There is no sign of layerwise delamination in any of the FGM samples. A small fraction of residual porosity can be seen at the interfaces of HA-$BaTiO_3$-HA. SEM (EDS) analysis of HA, buffer (HA:$BaTiO_3$, HA:$CaTiO_3$), $BaTiO_3$ and $CaTiO_3$ layers reveal no transfer of material through the interfaces. Overall, it can be suggested that the buffer has significantly reduced thermal stresses between HA and $BaTiO_3$ layers as well as HA and $CaTiO_3$ layers.

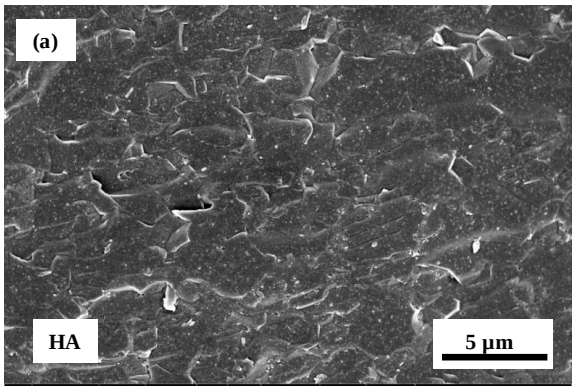
(a)
HA
5 µm

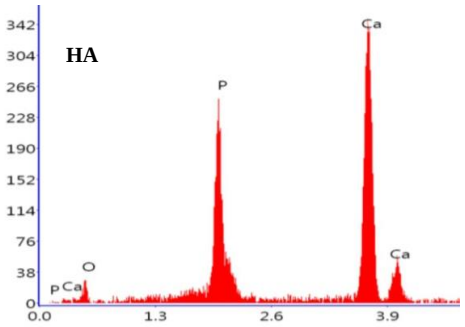
HA
342
304
266
228
190
152
114
76
38
0
P
Ca
O
Ca
Ca
0.0
1.3
2.6
3.9

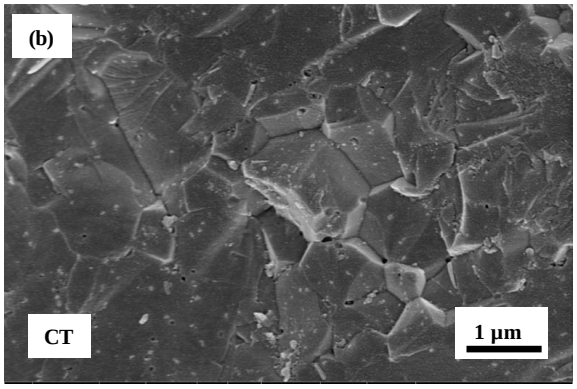
(b)
CT
1 µm

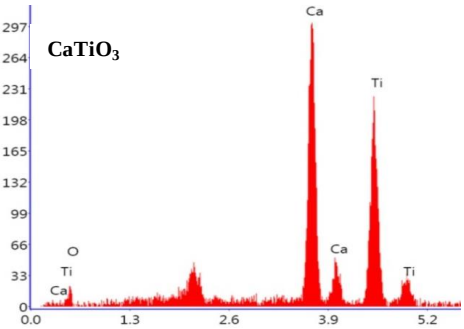
CaTiO3
297
264
231
198
165
132
99
66
33
0
Ca
Ti
O
Ti
Ca
Ca
Ti
0.0
1.3
2.6
3.9
5.2

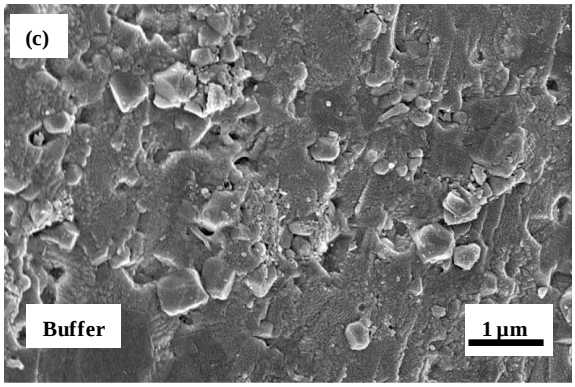
(c)
Buffer
1 µm

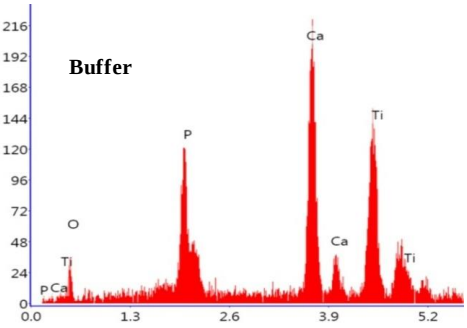
Buffer
216
192
168
144
120
96
72
48
24
0
Ca
P
Ti
O
Ca
Ti
Ti
Ca
0.0
1.3
2.6
3.9
5.2

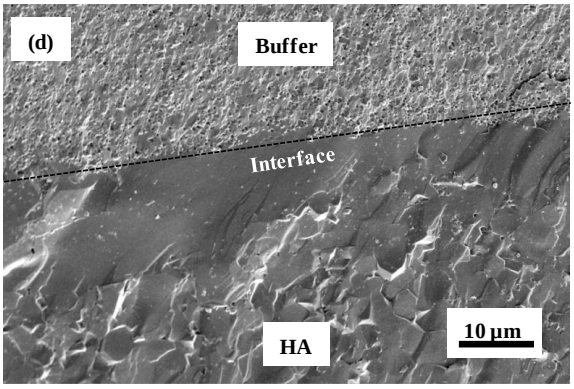
(d)
Buffer
Interface
HA
10 µm

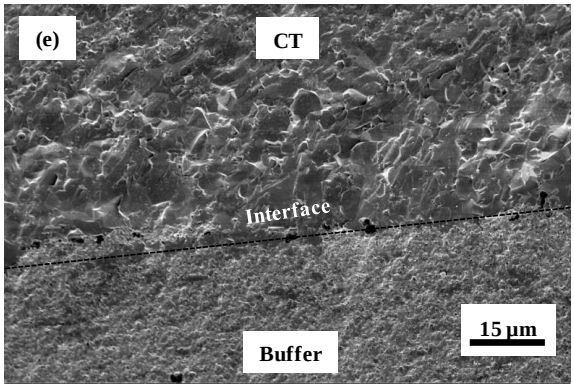
(e)
CT
Interface
Buffer
15 µm

HA

Element	Wt %	Atomic %	Error %
O K	22.39	40.02	17.83
P K	21.85	20.18	4.97
CaK	55.76	39.79	3.68

CT

Element	Wt %	Atomic %	Error %
O K	17.29	36.34	21.10
CaK	40.71	34.16	3.82
TiK	42.01	29.50	5.19

Buffer

Element	Wt %	Atomic %	Error %
O K	25.95	47.60	19.02
P K	9.94	9.42	7.81
CaK	30.80	22.56	5.68
TiK	33.32	20.42	5.95

Fig. 5.4: SEM micrographs illustrating the morphological behaviour of fractured surfaces of (a) HA, (b) CT and (c) buffer, interfacial regions between (d) HA and buffer as well as (e) CT and buffer.

5.3.2. Dielectric behaviour of HA and FGMs

Fig. 5.5 represents the variation of dielectric constant (ε) and loss (D) with temperature at few selected frequencies (1 kHz – 1 MHz) for HA, HA-BT-HA and HA-CT-HA compositions. It is observed that dielectric constant (ε) and loss (D) characteristics of HA [Fig. 5(a)] is appearing to be poorly dependent on temperature in the lower temperature range (< 200˚C). However, a diffused maxima is observed in the dielectric constant curve of HA (at 1 kHz) at about 100˚C, which is then followed by a linear increase with temperature. At higher frequencies (> 1 kHz), this characteristic fades. The dielectric loss curve almost depicts the similar behaviour. The diffused maximum (at 1 kHz) is associated with the loss of surface bound water molecule.[23] Further, with increase in temperature, dielectric curve shows dispersive nature at low frequency (< 100 kHz). Whereas, at higher frequencies (> 100 kHz), dielectric characteristics are weakly dependent on temperature within our measuring temperature range. In the apatite structure, the hydroxyl ions (OH^-) are weakly bound in the

lattice and are oriented perpendicularly to the Ca^{2+} triangles along c-axis.[24] These dipoles can be aligned with externally applied electric field and conduction occurs due to migration of protons (H^+).[25] At elevated temperature (> 300˚C), the higher dispersion in the curve [Fig. 5(a)] is seemingly due to the generation of the thermal defects. In lower temperature regions (100˚C - 300˚C), HA exhibits the structural instability where the transition from monoclinic (crystallographic space group: $P2_1/b$) to hexagonal ($P6_3/m$) phase occurs at 200˚C with majority of OH^- ions oriented in the same direction.[24,26]

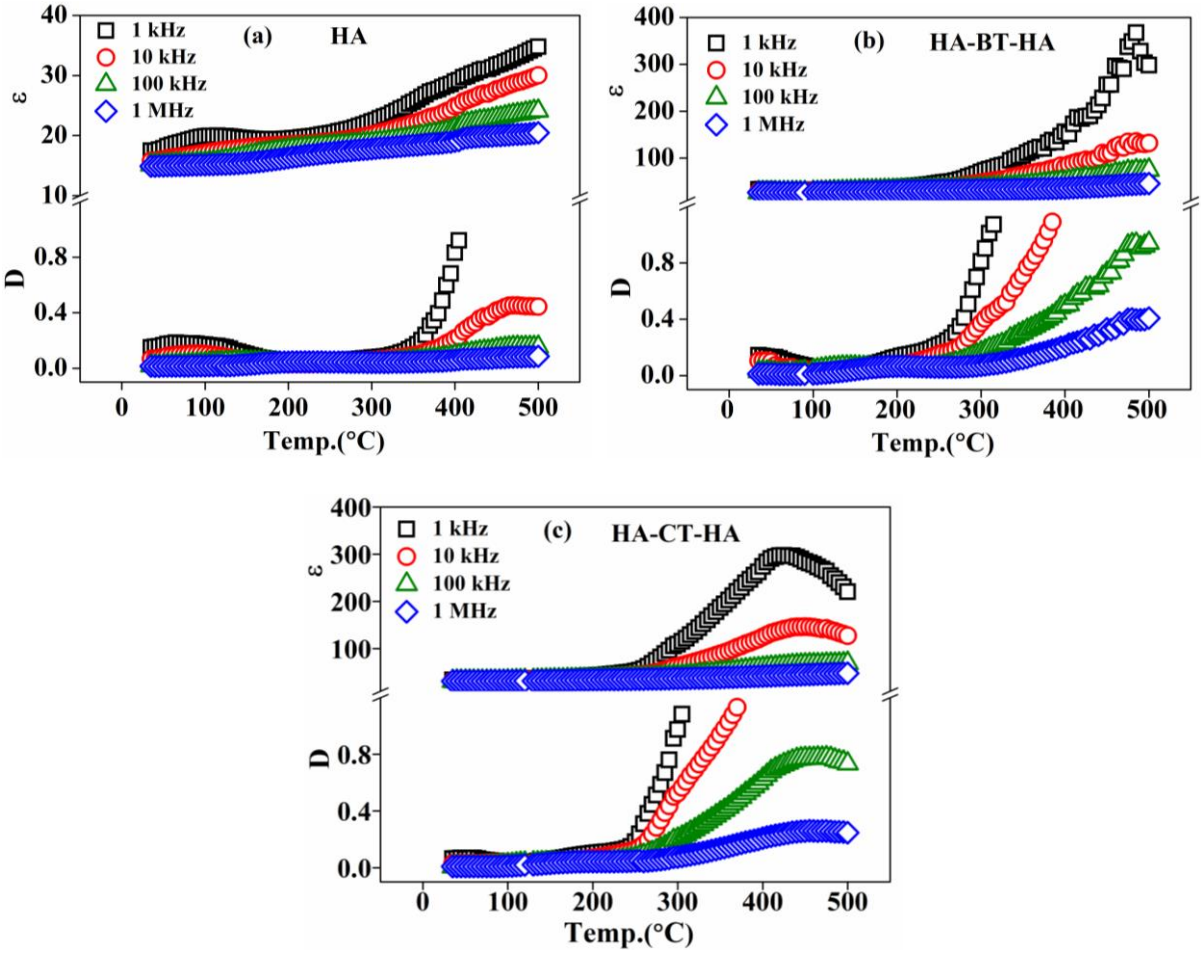

Fig. 5.5: Variation of dielectric constant (ε) and loss (D) for (a) HA, (b) HA-BT-HA and (c) HA-CT-HA with temperature at few selected frequencies.

The presence of $BaTiO_3$ and $CaTiO_3$ in the FGM has substantially influenced the dielectric behaviour of HA [Figs. 5 (b) and (c)]. As depicted, the room temperature (35˚C) dielectric

constant values of HA-BT-HA (34) and HA-CT-HA (34) FGMs are 2 times higher than that of pure HA (17) at 1 kHz. The dielectric constant and loss are observed to be independent with temperature in the lower temperature range (< 200˚C) and depicts significant increase at higher temperatures (> 200˚C) [Figs. 5(b) and (c)]. The increase in dielectric constant and loss with temperature is more significant at lower frequencies (< 10 kHz) than at higher frequencies (> 10 kHz). Such dielectric behaviour can be associated with the presence of multiple interfacial regions and phases in the FGM. Number of phases and interfacial regions of different electrical conductivities gives rise to interfacial polarization. In addition, dielectric constant and loss decreases with increase in frequency and at higher frequencies (≥ 100 kHz), almost independent nature of the curve with temperature is observed in the measuring temperature range. Further, there is an anomaly in dielectric constant in the temperature range of 400˚C - 500˚C. This is credited to the creation of oxygen vacancy in titanates (owing to variable valency of Ti, i.e. Ti^{4+}/Ti^{3+}), at high temperature (> 400˚C), which can be depicted as,[27]

$$O_o^* \leftrightarrow V_o + \frac{1}{2}O_2 \uparrow \quad (5.2)$$

$$V_o \leftrightarrow V_o^{\cdot\cdot} + 2e' \quad (5.3)$$

$$Ti^{4+} + e' \leftrightarrow Ti^{3+} \quad (5.4)$$

The creation of double positive charge as the electronegative oxygen leaves the lattice sites, creates defects, which enhances the ionic and electronic conduction at high temperature in the material.

Fig. 5.6 demonstrates the variation of dielectric constant and loss with frequency at few selected temperatures for HA, HA-BT-HA and HA-CT-HA compositions. At elevated temperatures (> 300˚C), the dielectric constant and loss are higher as compared to lower temperature region (< 200˚C) in HA [Fig. 5.6 (a)]. Higher temperature region of the dielectric constant corresponds to the thermal defects, formed in the OH^- sites due to dehydroxylation

in the bulk material.[24,28] In addition, higher temperature region (> 300˚C) also corresponds to the alignment of the OH^- ions together with space charge polarization.[23] The lower temperature region is associated with structural defects during processing and proton conduction due to the adsorbed water content.[24,28]

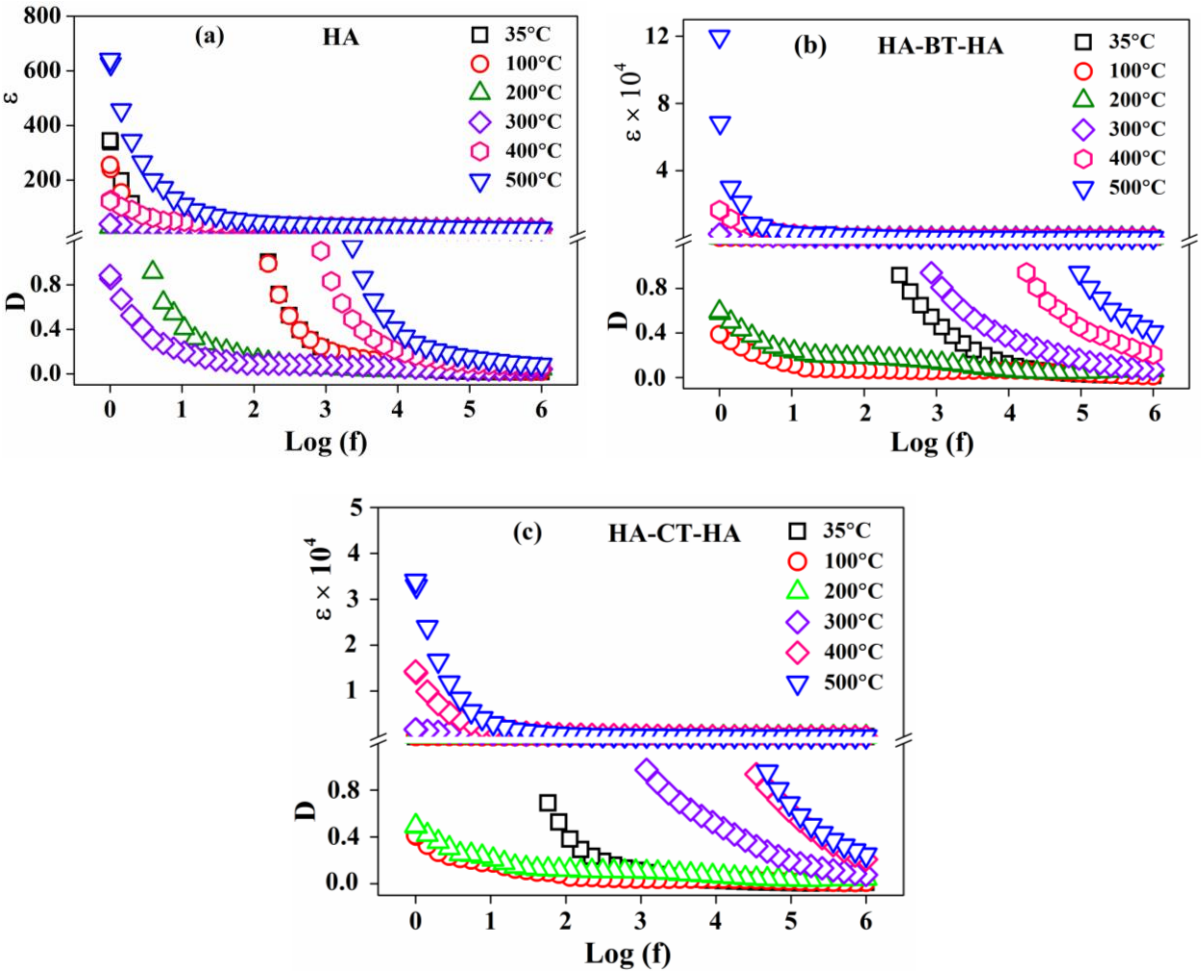

Fig. 5.6: Variation of dielectric constant (ε) and loss (D) for (a) HA, (b) HA-BT-HA and (c) HA-CT-HA with frequency at few selected temperatures.

Higher dielectric loss in lower frequency range (< 10^2 Hz) and at elevated temperatures (> 300˚C) is attributed to the dc conductivity in HA.[29] Further, with increase in frequency, dielectric constant and loss decreases which represents the relaxation of space charge through grain boundaries as well as dipolar relaxation due to the non-alignment of OH groups in lattice.[7] In high frequency range (> 10^3 Hz), dielectric constant and loss characteristics are

independent with frequency irrespective of the temperature, owing to the relaxation of polarization processes in the material.[23]

As is clearly depicted in Figs. 5.6 (b) and (c), dielectric constant and loss have larger dispersion in the lower frequency range (up to 10^2 Hz), specifically at 500˚C. However, almost frequency independent behaviour is observed in the higher frequency region (> 1 kHz), irrespective of the temperature. This type of behaviour is indicative of the Maxwell-Wagner type relaxation occurring in such heterogeneous systems.[30] As mentioned, FGMs are having multiple dielectrics, stacked layer by layer and therefore, there is a large amount of potential barrier existing at the interfacial region. In addition to grain boundaries, interfacial regions also act as a region of space charge. Under the influence of electric field, effect of space charge is dominant at low frequencies (< 10 Hz) and elevated temperatures (> 300˚C), resulting in higher dielectric constant. At low frequency, higher resistances of grain boundaries and interfacial regions result in higher dielectric loss [Figs. 5.6 (b) and (c)]. As the frequency increases, space charge polarization seizes to align with the field resulting in the decrease in dielectric constant. The reduction in the resistance of grain boundaries and the interfacial region results in lower dielectric loss, as depicted.

5.3.3. AC conductivity behaviour of HA and FGMs

Fig. 5.7 represents the variation of ac conductivity with temperature at few selected frequencies (1 kHz - 1 MHz) for HA, HA-BT-HA and HA-CT-HA samples. A general observation is that the conductivity increases linearly at elevated temperatures (> 300˚C) after a diffused maxima. The maxima correspond to the relaxation behaviour in the samples. With increase in temperature, the maxima shift towards the higher temperature region. The linear increase in conductivity at high temperatures, follows the Arrhenius equation, $\sigma = \sigma \exp(E_a/kT)$, where E_a is the activation energy for conduction. The conduction in HA at elevated temperature (> 300˚C) follows the process of de-hydroxylation i.e., removal of one

OH^- ion and one H^+ (proton) ion from two OH^- lattice sites as water molecule which creates defect.[25] The creation of the vacancy at one of the hydroxyl (OH^-) site and oxide ions in another OH^- site is mainly responsible for the increased conductivity at elevated temperature. The downfall in the curve with increase in temperature (200˚C - 300˚C) is attributed to the dehydration of the water molecule, strongly physisorbed with HA [Fig. 5.7(a)].[28] Also, high temperature induced defects in buffer (HA-BT/HA-CT), $BaTiO_3$, $CaTiO_3$ and at the interfacial regions contributes to the increase in conductivity with temperature [Figs. 5.7(b) and (c)] as compared with that of pure HA.

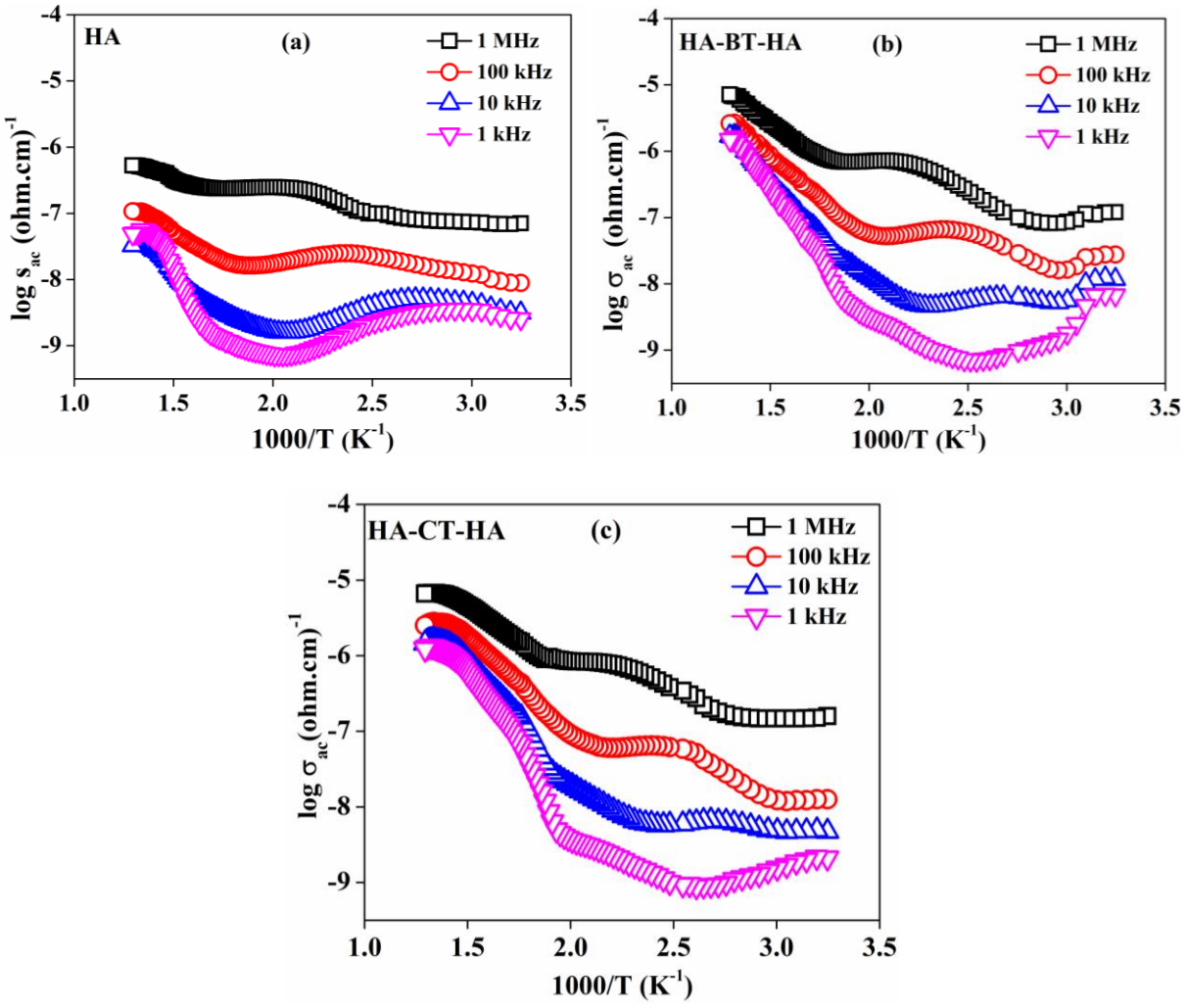

Fig. 5.7: Variation of AC conductivity for (a) HA, (b) HA-BT-HA and (c) HA-CT-HA with temperature at few selected frequencies.

HA possesses hexagonal close packed structure with hydroxyl ions (OH^-) located centrally around Ca^{2+} triangles along c-axis.[31] The electrical property of HA is majorly influenced by the presence/movement of proton (H^+), oxide ions (O^{2-}) and hydroxyl ions (OH^-), while the Ca^{2+} and PO_4^{3-} barely participate in its conductivity.[32] The presence of hydroxyl ions (OH^-) along the c-axis plays a significant role in ionic conduction and therefore, HA is considered as the one dimensional anionic conductor.[28,32,33] Proton conduction between neighbouring OH^- ions (0.344 nm) [$OH^- + OH^- \rightarrow O^{2-} + H_2O$] is considered as one of the conduction mechanisms,[25,28,32] while other mechanism includes proton jump between adjacent OH^- ions through PO_4^{3-} as they are in close proximity (0.307 nm) with the OH^- ions in the lattice [$2OH^- + PO_4^{3-} \rightarrow O^{2-} + HPO_4^{2-} + OH \rightarrow O^{2-} + PO_4^{3-} HOH + \square_{OH^-}$, □ indicates vacancy at OH^- lattice site, O^{2-} is oxide ion converted from OH^- ion].[34,35] At elevated temperatures, decomposition of OH^- ions [$Ca_{10}(PO_4)_6(OH)_2 \rightarrow Ca_{10}(PO_4)_6(OH)_{2-2x}O_x(\square)_x + H_2O(g)\uparrow$, □ indicates vacancy] from the lattice forms vacancy at the centre of the Ca^{2+} triangles which affects the conduction in HA.[35] In essence, at lower temperatures (< 100˚C), proton (H^+) conduction due to hydration in HA is proposed to be a dominant feature, while at elevated temperature (> 200˚C), hydroxyl ions (OH^-) and the hopping of protons at the O^{2-} sites are the main contributors to the conductivity of HA.[28]

Fig. 5.8 demonstrates the variation of ac conductivity with frequency at few selected temperatures. In case of HA [Fig. 5.8(a)], the ac conductivity is observed to be independent of frequency in the lower frequency range (< 10^2 Hz) at elevated temperatures (> 300˚C), while a quasi linear nature is noted at low temperatures (< 200˚C). As frequency increases beyond a particular threshold (> 10^3 Hz), the ac conductivity follows the 'universal' power law behaviour as,[36]

$$\sigma(\omega) = \sigma(0) + A\omega^n \qquad (5.5)$$

Where, ω, n and $\sigma\ (0)$ are the angular frequency, a constant ($0 < n < 1$) and the low-frequency conductivity, respectively. Low frequency conductivity [σ (0)] in the sample is mainly due to excitation of electrons from localized state to conduction bands. The exponent n is the degree of interaction between mobile ions and the lattice and A is the strength of polarizability. This type of conductive behaviour is shown to be of R-C type (resistor-capacitor).[37,38,39] In HA, the arrangement of OH^- ions along the channels of the Ca^{2+} triangles is responsible for conductive behaviour of HA, while the capacitive behaviour is shown by the immobile ions i.e., phosphate ions (PO_4^{3-}) and calcium ions (Ca^{2+}). In the low frequency region, ac conductivity of HA falls with rise in temperature upto 300˚C. This behaviour is mainly attributed to the loss of the water molecules from HA, as proposed by Nagai et al.[28] As the temperature rises above 300˚C, an increase in the ac conductivity in the low frequency region is observed, which is mainly due to the de-hydroxylation of OH^- ions that forms the conductive channels, owing to defects in the HA structure.[32]

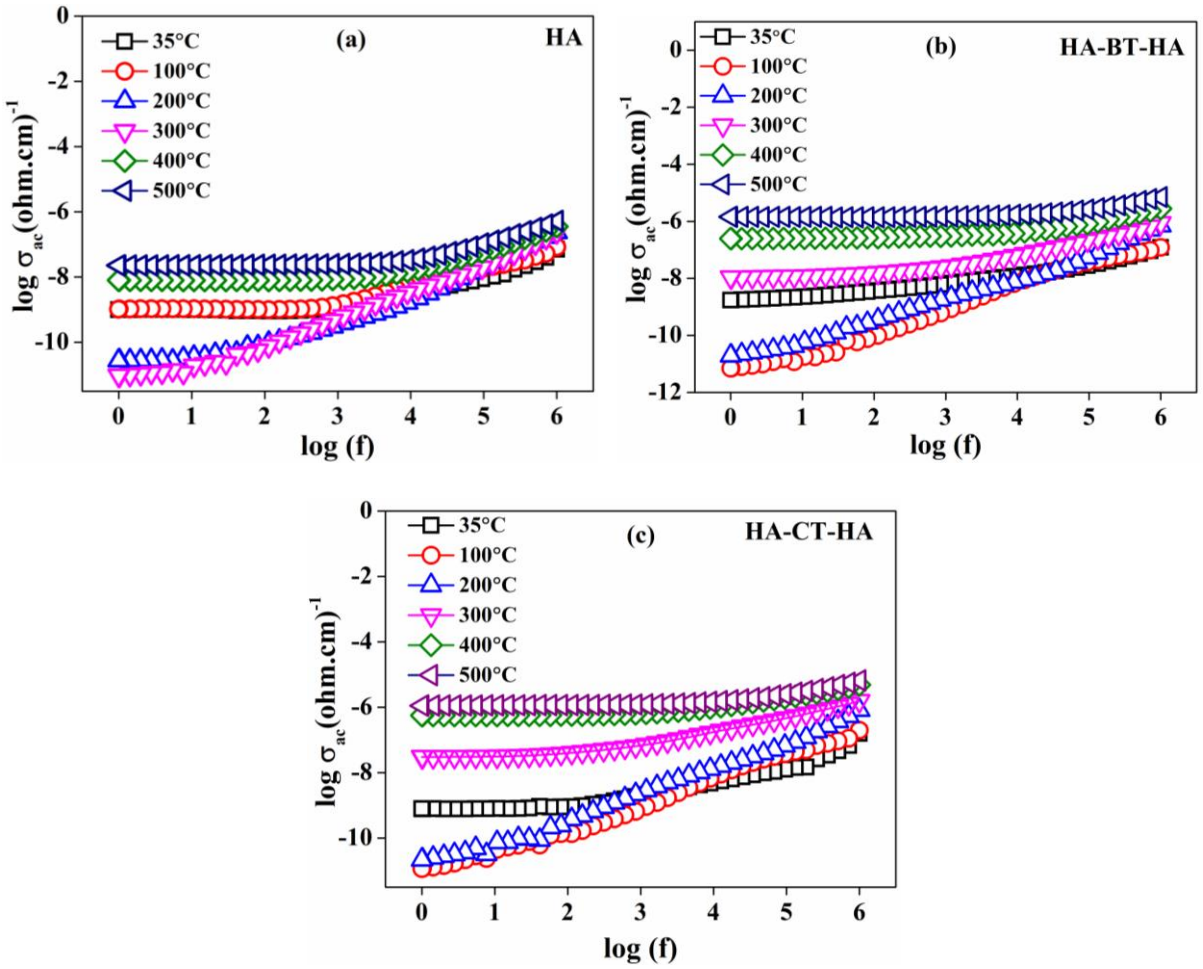

Fig. 5.8: Variation of AC conductivity for (a) HA, (b) HA-BT-HA and (c) HA-CT-HA with frequency at few selected temperatures.

In case of FGMs [Figs. 5.8 (b) and (c)], the conductivity increases with increase in frequency. At lower temperature region (< 100˚C), conductivity is almost independent of frequency upto 10^2 Hz and increases linearly with further increase in frequency. However, for higher temperatures (> 200˚C), conductivity shows marginal increase with frequency as compared to a constant linear increase for temperatures in the range of 100˚C - 200˚C. This behaviour appears to follow the Jonscher's power law.[36] The resistive behaviour in the FGMs can be suggested to be associated with the conduction of charge carriers, created via defects in HA, $BaTiO_3$, $CaTiO_3$ and buffer regions and capacitive behaviour is due to space charge region in vicinity of grain boundaries and interfacial regions.[7] The frequency at which the conductivity

shows a significant rise in each curve is known as hopping frequency.[40] This hopping frequency is depicted to be shifted in each curve towards higher frequency as temperature increases. As can be seen in FGMs [Fig. 5.8(b) and (c)], the steepness of the curve decreases with increasing frequency for higher temperatures (> 200˚C), this behaviour can be analysed using the CBH (Correlated Barrier Height) model.[41] The model emphasises on the role of quasi particles, called polarons, which are heavy charge particles created by the distortion of the lattice under the applied electric field and are responsible for the conduction in the solids. Accordingly, the conduction occurs due to the hopping of polarons between charged defects, separated by potential barrier.[40,41] The separation between the defects is mainly attributed to the Coulombic interaction which is comparable to the potential barrier height. This conduction mechanism is of translational type, which is hopping of the charge carriers i.e., proton and OH^- hopping in case of HA and creation of the oxygen vacancy at higher temperature for $BaTiO_3$ and $CaTiO_3$.[27,28] Further, the decrease in steepness in conductivity behaviour with rise in temperature is attributed to decrease in binding energy, required to create the oxygen vacancy and OH^- defects in the lattice.[42]

5.3.4. Impedance analysis

The impedance spectroscopy / electrochemical impedance spectroscopic (EIS) is an electrical characterization technique to separate out the combined complex electrical contributions from different phases, compositions, defects structures, dopants, etc. exists in a bulk solid electrolyte. Thereafter, these individual electrical characteristics can further be analysed / modified for the desired applications. In this technique, ac voltage / current is applied across the sample and subsequently, the output voltage / current is measured. The ac input voltage / current varies over wide frequency range (typically between: 10^{-2} Hz - 10^7 Hz). The output voltage / current can be out of phase or in-phase depending on the impedance of the sample as well as source frequency. Subsequently, impedance of the sample is evaluated which

contains resistive, capacitive or inductive contributions. The evaluation is repeated for each source frequency. The impedance of the sample is then a function of source frequency. Different constituents in the sample are then represented by resistance and reactive (capacitive) component (generally in parallel combination). Finally, these constituents are studied / analysed by evaluating their time constant ($\tau = RC$) / relaxation time. The impedance spectroscopic curve is a semicircular plot in a complex plane (Nyquist plot) between reactive (capacitive; imaginary, Z'') and resistive (real, Z') components. This semicircular plot is a combination of different semicircles for each constituent in the sample such as bulk material, grain boundaries and interfacial regions. The left side of the entire plot is a high frequency region and right side is a low frequency region.

The impedance plots as complete semicircular arcs with their centre on the abscissa, represented by parallel RC circuit, refer to the ideal Debye - type behaviour of the material. However, the real materials do not exhibit ideal Debye - type behaviour. Therefore, in order to illustrate the deviation from the ideal behaviour, the constant phase element (CPE) is introduced in place of ideal capacitor into the equivalent circuit.[43] CPE is used to explain the diffusion processes, stress and inhomogeneous behaviour in the grain boundary regions and the bulk.[44] In addition, CPE represents the dependence of impedance on frequency in high frequency region, following the Jonscher's power law.[36] The CPE values have been calculated using the expression, $C=(R^{1-n}C_Q)^{1/n}$; where, the parameters C_Q and n are used to define CPE (R and C_Q are the resistance and capacitance, respectively, $n > 0$ for non-ideal case).[45] The impedance analysis reveals the electrical contributions from grain, grain boundary and sample-electrode interface in terms of their resistances and CPE. Therefore, each constituent can be represented as parallel combination of resistance and CPE. The contribution of sample-electrode interface is negligible in most of the cases that is why double R-CPE circuits in series are used to represent grain and grain boundary contributions.

Each R and CPE combination (parallel) has a time constant which depicts the relaxation behaviour of the circuit. The maxima of a particular semicircular arc represent the point of relaxation frequency of a single R-CPE circuit. The relaxation frequency can be obtained as, $\omega\tau_r = (2\pi f_r RC) = 1$, where τ_r is the time constant of the R-CPE circuit.[46]

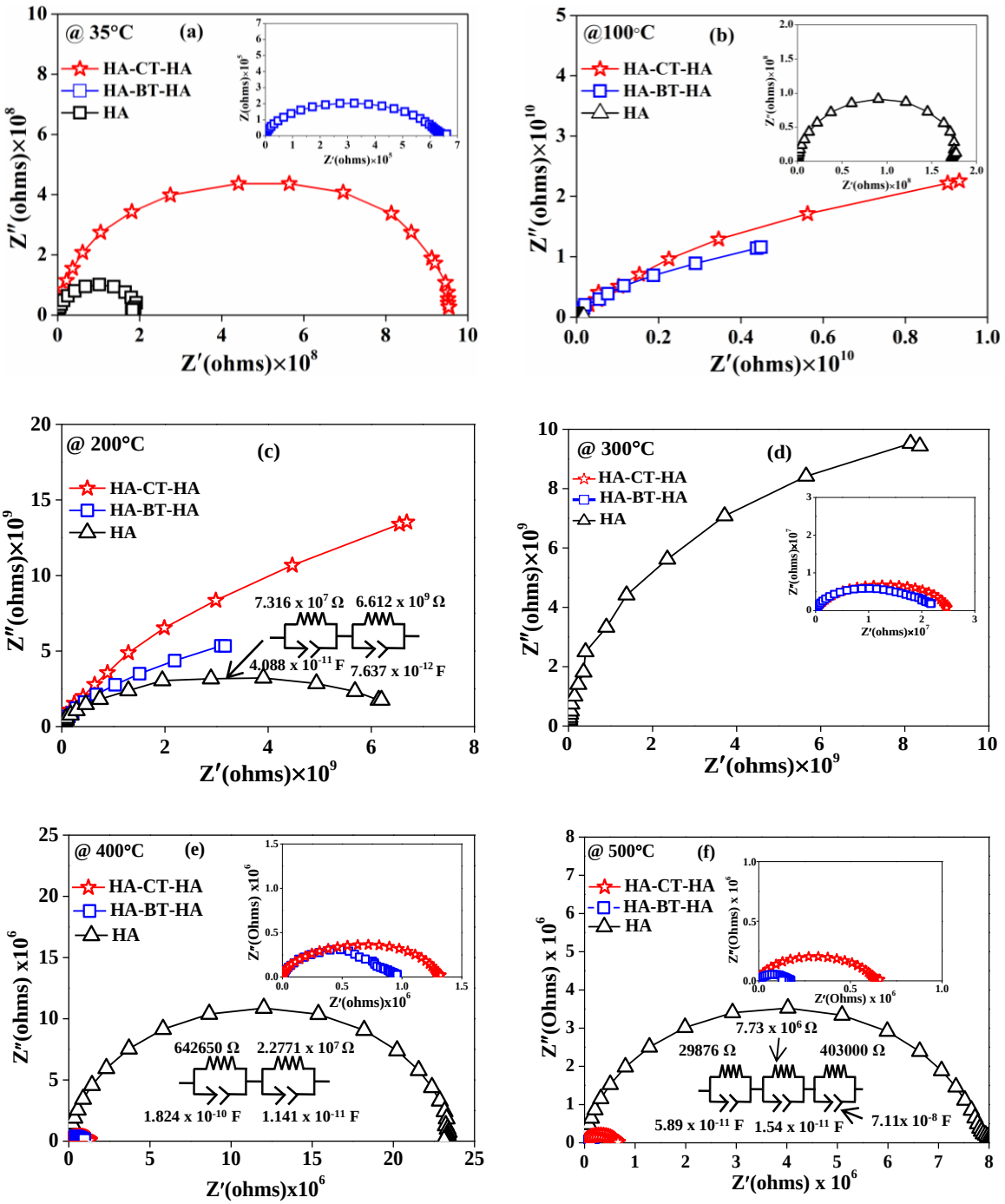

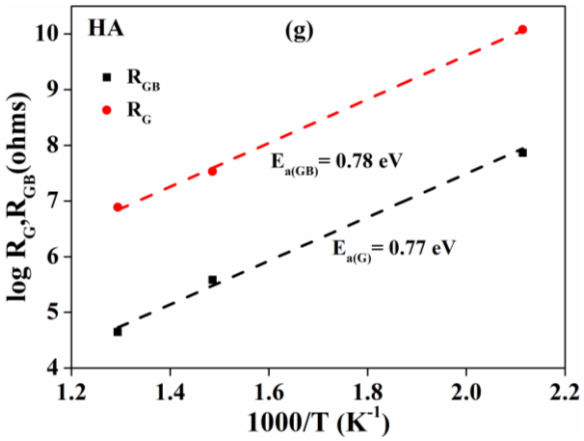

Fig. 5.9: Complex plane impedance plots for HA, HA-BT-HA and HA-CT-HA at few selected temperatures (a-f). Variation of resistances of grain (R_G) and grain boundary (R_{GB}) with inverse of temperature (g).

As can be seen in case of HA [Figs. 5.9 (a), (b) and (c)], the real and imaginary parts of the complex impedance increases with increase in temperature upto 300˚C. This is due to the release of water molecules from the sample at lower temperature region (< 200˚C) which plays a dominant role to hinder its conductivity, as reported by Nagai et al.[28] As temperature further increases, the real and imaginary parts of the complex impedance of HA decreases, which is mainly attributed to the defects at the OH^- and O^{2-} lattice sites in the sample.[25] In the lower temperature region (< 300˚C), the peaks in HA curve are observed to shift towards lower frequency region which can be due to the higher resistance of grain boundaries. For FGM (HA-BT-HA and HA-CT-HA), impedance plots depict high values of real and imaginary parts of impedance at low temperature (< 300˚C) due to the presence of different phases in the sample [Figs. 5.9 (a), (b) and (c)]. The presence of interfacial layer between different compositions in the FGM, acts as a region of space charge. It is also depicted that the semicircular arcs of FGM are asymmetric which reveal the contribution of different phases/composition with distinct conductivities in the sample. Above 300˚C, there is a substantial decrease in the values of real and imaginary parts of the impedance for HA-BT-HA [Figs. 5.9 (d) and (e)] and HA-CT-HA, suggesting that there is significant effect of grain

boundaries, interfacial regions, creation of oxygen vacancies and proton conduction in all the compositions, stacked layer by layer.[27,28] The shift of the relaxation peaks towards higher frequency region as temperature increases is mainly associated with the mobility of space charge and creation of oxygen vacancies.[46] At 500°C, [Fig. 5.9 (f)] the impedance plot is depicting the additional contribution apart from grain and grain boundaries in the much lower frequency region. This contribution is associated to be the interface between sample and electrode as the CPE value is depicted to be in the range of 10^{-8} F.[47] This is mainly because of the charge build-up at the interface between HA and electrodes and is due to the bulk ionic conduction in HA associated with the dehydroxylation process as well as proton (H^+) conduction occurring at higher temperatures. In case of FGMs, the resistance is fairly decreased due to the additional contributions from charge build-up at interfacial regions and also due to the migration of oxygen vacancies in BT and CT constituent phases. The activation energies, calculated from the linear fit in the log (R_G, R_{GB}) vs. 1000/T plot [Fig. 5.9 (g)], for grain [$E_{a(G)}$] and grain boundary [$E_{a(GB)}$] in HA are 0.77 eV and 0.78 eV, respectively. Therefore, the conduction in HA can be suggested to be associated with the conduction of protons (H^+) and structural defects created due to oxygen vacancies.[48]

5.4. Summary

The concept of development of Functionally Graded Materials using perovskites $BaTiO_3$ and $CaTiO_3$ as intermediary layers between hydroxyapatite (HA) layers via buffer interlayers significantly improved the polarizability of hydroxyapatite without any effect on its excellent biocompatibility. The insertion of buffer interlayers between hydroxyapatite and $BaTiO_3$/$CaTiO_3$ layers as well as processing via spark plasma sintering route provided good thermochemical stability as well as structural integrity to the developed FGM. Such a design and processing concept doubled the polarizability of hydroxyapatite. The proton conduction, hoping of charged carriers via oxygen vacancies and dehydroxylation of hydroxyapatite have

been observed as dominant mechanisms in the measured temperature range. Overall, the developed FGM can be suggested as potential alternative for polarizable bone application.

References

[1] M. H. Fathi, V. Mortazavi and S. I. R. Esfahani, "Bioactivity evaluation of synthetic nanocrystalline hydroxyapatite", *Dental Research Journal*, 5(2), (2008), 81-87.

[2] A. Sobczak, Z. Kowalski and Z. Wzorek, "Preparation of Hydroxyapatite from animal bones", *Acta of Bioengineering and Biomechanics*, 11 (4), (2009), 23-28.

[3] B. Basu, D. S. Katti and A. Kumar, Advanced Biomaterials: Fundamentals, Processing and Applications, John Wiley and Sons, New Jersey (2009).

[4] N. C. Teng, S. Nakamura, Y. Takagi, Y. Yamashita, M. Ohgaki and K. Yamashita, "A New Approach to Enhancement of Bone Formation by Electrically Polarized Hydroxyapatite", *Journal of Dental Research*, 80 (10), (2001), 1925-1929.

[5] A. Ravalioli and A. Kraiewski, Bioceramic: Materials, Properties, Applications, Chapman & Hall, London (1992).

[6] E. Fukada and I. Yasuda, "On the piezoelectric effect of bone", *Journal of the Physical Scoiety of Japan*, 12(10), (1957), 1158-1162.

[7] A.K. Dubey, K. Kakimoto, A. Obata, and T. Kasuga, "Enhanced polarization of hydroxyapatite using the design concept of functionally graded materials with sodium potassium niobate", *RSC Advances*, 4(47), (2014), 24601-24611.

[8] C. A. L. Bassett, "Electrical effects in bone", *Scientific American*, 213 (4), (1965), 18-25.

[9] Y. J. Park, Y. H. Jeong, Y. R. Lee, S. R. Noh and H. J. Song, "Effect of Negatively Polarized Barium Titanate Thin Film, Formed on Ti, on Osteoblast Cell Activity", *Journal of Dental Research*, 82, (2003), B212.

[10] J. Q. Feng, H. P. Yuan, and X. D. Zhang, "Promotion of Osteogenesis by a Piezoelectric Biological Ceramic", *Biomaterials*, 18, (1997), 1531-1534.

[11] Y. J. Park, K. S. Hwang, J. E. Song, J. L. Ong, and H. R. Rawls, "Growth of Calcium Phosphate on Poling Treated Ferroelectric $BaTiO_3$ Ceramics", *Biomaterials*, 23, (2002), 3859-3864.

[12] K. S. Hwang, J. E. Song, H. S. Yang, Y. J. Park, J. L. Ong, and H. R. Rawls, "Effect of Poling Conditions on Growth of Calcium Phosphate Crystal in Ferroelectric $BaTiO_3$ Ceramics", *Journal of Materials Science: Materials in Medicine*, 13, (2002), 133.

[13] A. K. Dubey, B. Basu, K. Balani, R. Guo, and A. S. Bhalla, Dielectric and Pyroelectric Properties of HAp-$BaTiO_3$ Composites, *Ferroelectrics*, 423 [1], (2011), 63.

[14] A. K. Dubey, B. Basu, K. Balani, R. Guo, and A. S. Bhalla, "Multifunctionality of Perovskites $BaTiO_3$ and $CaTiO_3$ in a Composite with Hydroxyapatite as Orthopedic Implant Materials", *Integrated Ferroelectrics*, 131(1), (2011), 119-126.

[15] X. M. Chen and B. Yang, "A New Approach for Toughening of Ceramics", *Materials Letters*, 33, (1997), 237-240.

[16] M. M. Beloti, P. T. de Oliveira, R. Gimenes, M. A. Zaghete, M. J. Bertolini, and A. L. Rosa, "In Vitro Biocompatibility of a Novel Membrane of the Composite Poly (Vinylidene-Trifluoroethylene)/Barium Titanate", *Journal of Biomedical Materials Research Part A*, 79A(2), (2006), 282-288.

[17] A. K. Dubey and B. Basu, "Pulsed Electrical Stimulation and Surface Charge Induced Cell Growth on Multistage Spark Plasma Sintered Hydroxyapatite - Barium Titanate Piezobiocomposite", *Journal of the American Ceramic Society*, *97* (2), (2013), 481-489.

[18] A. K. Dubey, G. Tripathi and B. Basu, "Characterization of hydroxyapatite perovskite ($CaTiO_3$) composites: Phase evaluation and cellular response", *Journal of Biomedical Materials Research Part B: Applied Biomaterials*, 95B, (2010), 320-329.

[19] T. J. Webster, C. Ergun, R.H. Doremus and W.A. Lanford, "Increased osteoblast adhesion on titanium-coated hydroxylapatite that forms $CaTiO_3$", *Journal of Biomedical Materials Research Part A*, 67, (2003), 975-980.

[20] P. K. Mallik and B. Basu, "Better early osteogenesis of electroconductive hydroxyapatite – calcium titanate composites in a rabbit animal model", *Journal of Biomedical Materials Research Part A*, 102 (3), (2013), 842-851.

[21] A. K. Dubey, P. K. Mallik, S. Kundu, B. Basu, "Dielectric and electrical conductivity properties of multi-stage spark plasma sintered HA–CaTiO3 composites and comparison with conventionally sintered materials", *Journal of the European Ceramic Society*, 33(15), (2013), 3445-3453.

[22] Zurkentnis R W de Phosphate : I. Uber Hydroxyapatite. BodenKflernah 12, (1939), 121-138.

[23] V. P. Orlovskii, N. A. Zakharov and A. A. Ivanov, "Structural transition and dielectric characteristics of high-purity hydroxyapatite", *Inorganic Materials*, 32(6), (1996), 654-656.

[24] N. A. Zakharov and V. P. Orlovskii, "Dielectric characteristics of biocompatible $Ca_{10}(PO_4)_6(OH)_2$ ceramics", *Technical Physics Letters*, 27 (8), (2001), 629-631.

[25] K. Yamashita, K. Kitagaki and T. Umegaki, "Thermal Instability and Proton Conductivity of Ceramic Hydroxyapatite at High Temperatures", *Journal of the American Ceramic Society, 78* (5), (1995), 1191-1197.

[26] H. Suda, M. Yashima, M. Kakihana and M. Yoshimura, "Monoclinic .tautm. Hexagonal Phase Transition in Hydroxyapatite Studied by X-ray Powder Diffraction and Differential Scanning Calorimeter Techniques", *The Journal of Physical Chemistry, 99* (17), (1995), 6752-6754.

[27] K. Kobayashi, Y. Doshida, Y. Mizuno and C. A. Randall, "A Route Forwards to Narrow the Performance Gap between PZT and Lead-Free Piezoelectric Ceramic with Low Oxygen Partial Pressure Processed $(Na_{0.5}K_{0.5})NbO_3$", *Journal of the American Ceramic Society*, 95(9), (2012), 2928-2933.

[28] M. Nagai and T. Nishino, "Surface conduction of porous hydroxyapatite ceramics at elevated temperatures", *Solid State Ionics*, 28-30, (1998), 1456-1461.

[29] J. P. Gittings, C. R. Bowen, I. G. Turner, F. Baxter and J. Chaudhuri, "Characterisation of ferroelectric-calcium phosphate composites and ceramics", *Journal of the European Ceramic Society, 27* (13), (2007), 4187-4190.

[30] E. Barsoukov, J. R. Macdonald, *Impedance Spectroscopy Theory, Experiment and Applications*, 2nd ed., Wiley-Interscience Press, New York (2005).

[31] M. I. Kay, R. A. Young and A. S. Posner, "Crystal Structure of Hydroxyapatite", *Nature*, 204, (1964), 1050.

[32] J. P. Gittings, C. R. Bowen, A. C. E. Dent, I. G. Turner, F. R. Baxter and J. B. Chaudhuri, "Electrical characterization of hydroxyapatite-based bioceramics", *Acta Biomaterialia*, 5 (2), (2009), 743-754.

[33] K. Yamashita, H. Owada, T. Umegaki, T. Kanazawa and T. Futagami, "Ionic conduction in apatite solid solutions", *Solid State Ionics*, 28-30, (1988), 660-663.

[34] A. Laghzizil, N Elherch, A. Bouhaouss, G. Lorente, T. Coradin and J. Livage, "Electrical behaviour of hydroxyapatites $M_{10}(PO_4)_6(OH)_2$ (M=Ca, Pb, Ba)", *Materials Research Bulletin*, 36, (2001), 953-962.

[35] A. Laghzizil, N. Elherch, A. Bouhaouss, G. Lorente and J. Macquete, "Comparison of electrical properties between fluoroapatite and hydroxyapatite materials", *Journal of Solid State Chemistry*, 156, (2001), 57-60.

[36] A. K. Jonscher, "The "Universal" dielectric response", *Nature*, 267, (1977), 673-679.

[37] B. Vainas, D P Almond, J. Luo and R. Stevens, "An evaluation of random R-C networks for modelling the bulk ac electrical response of ionic conductors", *Solid State Ionics*, 126, (1999), 65-80.

[38] D.P. Almond and B. Vainas, "The dielectric properties of random R-C networks as an explanation of the "universal" power law dielectric response of solids", *Journal of Physics: Condensed Matter*, 11, (1999), 9081-9093.

[39] CR Bowen and DP Almond, "Modelling the "universal" dielectric response in heterogeneous materials using microstructural electrical networks", *Materials Science and Technology*, 22, (2006), 719-724.

[40] M. Sindhu, N. Ahlawat, S. Sanghi, A. Agarwal, R. Dahiya and N. Ahlawat, "Rietveld refinement and impedance spectroscopy of calcium titanate", *Current Applied Physics*, 12 (6), (2012), 1429-1435.

[41] K. Prasad, S. Bhagat, K. Amarnath, S.N. Choudhary and K.L. Yadav, "Electrical conduction in $Ba(Bi_{0.5}Nb_{0.5})O_3$ ceramic: Impedance spectroscopy analysis", *Materials Science-Poland*, 28(2009), (2010), 317-325.

[42] N. Ortega, A. Kumar, P. Bhattacharya, S.B. Majumder and R.S. Katiyar, Impedance spectroscopy of multiferroic $PbZr_xTi_{1-x}O_3$／ $CoFe_2O_4$ layered thin films, *Physical Review B*, 77, (2008), 014111.

[43] A. R. West, D. C. Sinclair and N. Hirose, "Characterization of Electrical Materials, Especially Ferroelectrics, by Impedance Spectroscopy", *Journal of Electroceramics*, 1 (1), (1997), 65-71.

[44] J.-B. Jorcin, M. E. Orazem, N. Pébère and B. Tribollet, "CPE analysis by local electrochemical impedance spectroscopy", *Electrochimica Acta*, 51 (8), (2006), 1473-1479.

[45] X. Guo, W. Sigle and J. Maier, "Blocking Grain Boundaries in Yttria-Doped and Undoped Ceria Ceramics of High Purity", *Journal of the American Ceramic Society, 86* (1), (2004), 77-87.

[46] I. M. Hodge, M. D. Ingram and A. R. West, "Impedance and modulus spectroscopy of polycrystalline solid electrolytes", *Journal of the Electroanalytical Chemistry and Interfacial Electrochemistry*, 74 (2), (1976), 125-143.

[47] J.T.S. Irvine, D.C. Sinclair, and A.R. West, "Electroceramics: Characterization by Impedance Spectroscopy", *Advanced Materials*, 2: (1990), 132-138.

[48] C. H. Park, "Microscopic Study on Migration of Oxygen Vacancy in Ferroelectric Perovskite Oxide", *Journal of the Korean Physical Society*, 42, (2003), S1420-S1424.